MDPI

Article

Study of Unsymmetrical Magnetic Pulling Force and Magnetic Moment in 1000 MW Hydrogenerator Based on Finite Element Analysis

Jiwen Zhang [1], Xingxing Huang [2] and Zhengwei Wang [1,*]

1   State Key Laboratory of Hydroscience and Engineering, Department of Energy and Power Engineering, Tsinghua University, Beijing 100084, China; zhangjw21@mails.tsinghua.edu.cn
2   S.C.I. Energy, Future Energy Research Institute, Seidengasse 17, 8706 Zurich, Switzerland; xingxing.huang@gmx.ch
*   Correspondence: wzw@mail.tsinghua.edu.cn

Abstract: The large dimensions of the 1000 MW hydroelectric generator sets require high mounting accuracy. Small deviations can lead to asymmetry, which in turn triggers unbalanced magnetic pulls and moments. Therefore, symmetry is a central challenge in the installation and operation of giant hydroelectric generators. In this paper, the effects of radial eccentricity, axial offset, and rotor shaft deflection on the unbalanced magnetic pull and moment are investigated by transient finite element analysis of the asymmetric magnetic field. The results of the time-domain and frequency-domain analyses show that asymmetric operation generates unbalanced magnetic forces and moments. These forces and moments increase linearly with increasing offset or deflection rate. When the eccentricity meets the installation criteria, the unbalanced magnetic pull forces are small and within acceptable limits. This study helps to understand the relationship between asymmetry and unbalanced magnetic pulling forces in large hydroelectric generators, and provides a theoretical basis for standardizing installation deviation control.

check for updates

1. Introduction

1.1. Background

As the core equipment for converting water energy into electricity, large hydrogenerators have an important position in the field of renewable energy [1–3]. With the transformation of the global energy structure and the enhancement of people's awareness of environmental protection and water energy as a clean, renewable energy, its development and utilization have received widespread attention. Large hydrogenerators can not only provide a stable power supply for industrial production and residential life but also reduce the use of fossil fuels and protect the environment.

However, in the actual operation of large hydrogenerators, rotor eccentricity is a problem that cannot be ignored. Rotor eccentricity may be caused by a variety of factors, such as manufacturing errors, improper installation or material wear, resulting in the rotor axis deviating from the ideal position. This phenomenon produces unbalanced magnetic tension and moments. This can exacerbate unit vibration [4–7] and noise [8,9], reduce power generation efficiency, and accelerate bearing wear. In severe cases, it may also lead to stator–rotor friction, causing safety accidents and posing a threat to the stable operation of the power system.

In summary, rotor eccentricity poses a serious threat to the safe operation during hydrogenerator operation. Therefore, we need to deeply study the mechanism of the rotor eccentricity's influence on unbalanced magnetic tension and magnetic moment, analyze the

law, and propose control measures. These studies are of great importance for improving the stability and safety of the operation of large hydrogenerators and promoting the sustainable development of renewable energy.

1.2. Research Status

Asymmetry is inevitable during the operation of the generator. The causes of asymmetry are mainly divided into three kinds: radial eccentricity of rotor, axial deviation and axial deflection. To be able to ensure the stable operation of the generator, it is needed to control the range of rotor installation deviation. The eccentricity will cause the air gap to be uneven, which will cause the asymmetric magnetic potential to be excited and produce an unbalanced magnetic pull (UMP). The UMP magnitude and distribution are strongly influenced by eccentricity. Depending on whether the air gap changes over time, eccentricity can be divided into static eccentricity and dynamic eccentricity. In the case of static eccentricity, the rotation of the generator rotor does not change the distribution of the air gap along the circumference. In this case, the rotor and shaft as a whole are offset relative to the stator, and the relative positions of the center points of the rotor and shaft are consistent. With dynamic eccentricity, the circumferential distribution of the air gap changes as the rotor rotates. Under normal circumstances, the position of the stator of the alternator is correct, but there is a shift in the relative position of the rotor and the center of rotation of the shaft. The eccentricity in UMP systems can lead to lateral displacement of the rotor, placing significant stress on the generator's radial guide bearings. This constant stress accelerates bearing wear, generates vibration and noise, and ultimately increases energy loss, reducing overall efficiency. In extreme cases, it can cause the rotor to rub against the fixed components, stopping the motor rotation and potentially leading to motor burnout. In addition, an uneven air gap can exacerbate voltage and current imbalances, reducing efficiency and creating safety hazards.

Therefore, evaluating the UMP over a range of eccentricity configurations is critical as highlighted in numerous conferences and research publications. Whilst a significant proportion of these studies have focused on smaller induction generators [7,9–17], this underlines the importance of understanding the effect of eccentricity on their performance. Certain investigations have focused on huge hydraulic systems, which inherently have a significant amount of poles and slots, as well as significant dimensions. These factors require a unique approach to assessing their UMP across different eccentric configurations [8,18–21]. The article [19] studies UMP under static eccentricity. Two-dimensional FEM and MST are used to study the relationship between magnetic tension and load. The article [20] develops a versatile magnetic force and rotor that can accommodate a wide range of external excitation frequencies, ensuring its applicability in different scenarios. This model differs from previous versions by emphasizing the significance of the UMP tangential component. As a result, the theory provides valuable insights into the design and analysis of generator rotors, allowing for more precise and optimized solutions. The reference [21] introduces a predictive method for assessing magnetic pull under mixed eccentricity conditions, to contribute to a better understanding of this phenomenon. A finite element analysis framework is constructed to simulate the electromagnetic flux and force dynamics, taking into account both rotor eccentricity and deformation. This approach generates UMP curves for two eccentricity scenarios, allowing predictions of the UMP behavior. Overall, these investigations focus primarily on the design of eccentricity models and the exploration of predictive methods in a two-dimensional context.

It is also essential to investigate the effects of UMP on generator performance. Its main effects are vibrations and deformations. The misalignment between the stator and the rotor results in fluctuations in the air gap dimension, which subsequently triggers the emergence of low-frequency vibrations and their harmonic components aligned with the rotor rotation cycle. This can potentially lead to the development of second-order (elliptical) or third-order (triangular) distortions, which have mechanical implications that need to be addressed [4]. In addition to eccentricity, the electromagnetic characteristics, including the excitation current

and the internal power angle, contribute significantly to shaping the intensity and distribution pattern of the UMP. Consequently, this force induces torsional vibrations along the rotor axis, the magnitude of which depends on the strength of the UMP itself [5]. The intensity of the magnetic field is intertwined with changes in the reactive load and damper windings, further influencing the unbalance response of the machine [22]. In particular, dynamic eccentricity-induced UMP in the stator–rotor system not only causes torsional vibrations of the rotor shaft but also vibrates the inclined stator frame. Such research is invaluable in diagnosing and resolving rotor asymmetry problems [6,19].

1.3. Research Overview

At present, the existing research focuses on the analysis of unbalanced magnetic pull and magnetic torque of small- and medium-sized induction motors under two-dimensional eccentricity. The influence of axial off-centeredness and unevenness on the distribution pattern of the EMF is not included in the current state of knowledge. Although many attempts have been made to model the three-dimensional EMF, the transient calculation of the three-dimensional EMF is often used in micro generators due to limitations in the calculation speed and accuracy. Like turbine generators or wind turbines, their size is mostly at the centimeter level. The calculation and analysis of UMP under 3D eccentricity is a major challenge for large hydrogenerators, given the accuracy and power of existing computers.

In this paper, a three-dimensional eccentric model is used to calculate the UMP and unbalance magnetic torque of hydrogenerators. Considering the radial eccentricity, axial deflection and axial deflection, the relationship between the distribution of UMP and unbalanced magnetic torque and the type and amount of eccentricity is studied. Section 2 introduces the calculation method of the finite element and its application to the calculation of electromagnetic fields, magnetic tension, and magnetic moment. In Section 3, a full three-dimensional finite element model of a large hydrogenerator rotor is established. At the same time, the accuracy of the model is verified. In Section 4, the finite element calculation and analysis of radial eccentric magnetic tension and magnetic moment are carried out. In Section 5, the FE calculation and analysis of magnetic force and torque of rotor axial migration are carried out. In Section 6, the finite element analysis of rotor axial deflection magnetic force and magnetic moment is carried out. Section 6 summarizes the work of the full text. The innovation of this study lies in the establishment of full three-dimensional hydrogenerator radial and axial eccentricity models, which reveal the distribution law of unbalanced magnetic tension and magnetic torque from the three-dimensional perspective.

2. Materials and Methods

2.1. Finite Element Calculation

The finite element method (FEM) is a generalized numerical method for solving partial differential equations. The method involves breaking down a large system into smaller, simpler parts, which are known as finite elements. This is performed by constructing a mesh of objects in the spatial dimension, which has a finite number of points. For edge-valued problems, the formulation of the finite element method eventually produces a system of algebraic equations. The method first approximates the unknown function over the entire domain. It then integrates the simplified system of equations representing these finite elements into a comprehensive system that models the entire problem. In the end, by minimizing the error function using variational techniques, the FEM approximates the solution.

Finite element analysis (FEA) in engineering serves as a computational tool for engineering analysis, using mesh generation to break down complex problems into smaller elements and using software programmed with finite element algorithms. When applying FEA, complex problems are usually physical systems with underlying physics, such as the Euler–Bernoulli beam equation, the heat equation, or the Navier–Stokes equation. They are expressed as PDEs or integral equations.

The finite element analysis method is as follows:

(1) Firstly, the solution region is discretized into a finite number of subregions.

(2)   The governing equations for the classical subregion are derived.

(3)   We solve for the sum of all the elements in the domain. By synthesizing the subregion equations obtained in the previous step, the total system equation is obtained.

(4)   The final solution is obtained by solving the system equation.

The classical finite element partitioning method is as follows. For a one-dimensional problem, a line segment with two nodes is divided into a subregion. For two-dimensional problems, the triangular region composed of three nodes is generally divided into a subregion. It is also possible to divide a hexagonal region composed of six nodes into a subregion. This applies to higher-order problems. For three-dimensional problems, it is usually divided into tetrahedrons with four nodes, or hexahedrons with eight nodes.

2.2. Transient Electromagnetic Calculation

Given the presence of current in the generator, it is essential to include the current source when assessing its electromagnetic field. The vector magnetic potential acts as a bridge between the different components of the field. Assuming a uniform, linear and isotropic medium with an electrical source as the sole field source, the formulation of the vector magnetic potential equation can be derived from the fundamental principles of the A-v-A eddy current region:

$$\nabla \times 1/\mu \, \nabla \times \mathbf{A} + \sigma(\partial \mathbf{A}/\partial t + \nabla V) = \mathbf{J}_0 \tag{1}$$

where $\mathbf{J}_0$ represents the current density vector derived from the excitation, and $\mathbf{V}$ denotes the velocity of motion. Using the following equation,

$$\nabla \times \nabla \times \mathbf{A} = \nabla(\nabla \cdot \mathbf{A}) - \nabla^2 \mathbf{A} = -\nabla^2 \mathbf{A} \tag{2}$$

Equation (1) can be converted into another form:

$$\nabla^2 \mathbf{A} - \mu\sigma \frac{\partial \mathbf{A}}{\partial t} = -\mu \mathbf{J}_0 + \mu\sigma \nabla \, \mathbf{v} \tag{3}$$

Assuming that $\mathbf{A}$ remains constant along the z-axis and focusing only on its variation in the XY plane, the evaluation of the motor's electromagnetic force can be achieved by analyzing the results of two-dimensional electromagnetic field simulations. As a result, the only contributions to the components of $\mathbf{J}_0$ and $\mathbf{A}$ come from the z-axis:

$$\mathbf{J}_0 = J_{0Z}, \mathbf{A} = A_Z \tag{4}$$

Equation (3) can then be rearranged into the form below:

$$\frac{\partial^2 A_Z}{\partial x^2} + \frac{\partial^2 A_Z}{\partial y^2} - \mu\sigma \frac{\partial A_Z}{\partial t} = -\mu J_{0Z} + \mu\sigma \frac{\partial v_x}{\partial x} + \frac{\partial v_y}{\partial y} \tag{5}$$

The magnetic induction intensity $\mathbf{B}$ is then determined from the description of $\mathbf{A}$, which inherently includes both magnetic induction and velocity components:

$$\mathbf{B} = \nabla \times \mathbf{A} \tag{6}$$

Equation (5) can be used to derive the z-component of the vector magnetic potential, denoted as A_Z. Since the number of equations is insufficient to solve for all unknowns, the rotational dynamics of the generator is introduced as described in Equation (7) where J is the rotor moment of inertia, T_{em} is the calculated electromagnetic torque, T_{load} is the load torque of the generator, ω is the angular velocity, and λ is the damping coefficient of the generator:

$$J\frac{d\omega}{dt} + \lambda\omega = T_{em} + T_{load} \tag{7}$$

Boundary conditions are essential for solving the differential equations. When calculating the two-dimensional electromagnetic field, a significant part of the magnetic induction **B** is confined within the boundaries of the generator. Consequently, the vector magnetic potential outside the boundary is set to zero as shown in Equation (8):

$$A_z = 0 \tag{8}$$

In addition to the aforementioned boundary conditions for the vector potential, the calculation of the generator EMF requires the excitation current from the external circuit. The objective of this study is to determine the distribution of the electric potential (EMF) inside the motor under rated operating conditions. The rated excitation current of the motor is 3492 A. The generator is operated at the rated load, with the external circuit set to rated load. Using the equivalent circuit diagram, the stator coil voltage is set at 24 kV, and the load torque T_{load} is calculated as P_{load}/ω, where P_{load} is the generator load and ω is the angular velocity.

2.3. UMP Calculation

The electromagnetic force is generated by the interaction between the generator and the magnetic flux lines passing through the air gap. The intensity of this force at different points can be quantified by integrating the electromagnetic force density. There are three main methods for making these calculations: the Lorentz force approach, the principle of virtual work, and the use of the Maxwell stress tensor method. The methodology used in this study involves applying the Maxwell stress tensor approach due to its ability to provide detailed electromagnetic force calculations and distribution maps, facilitating further analysis of the hydrogenerator vibration issues. This methodology serves as the basis for the Unified Magnetic Potential (UMP) approach.

The magnetic flux density of the air gap is determined through the application of the permeance function $\Lambda(\theta, t)$ in conjunction with the magnetomotive force (MMF) f_{mm}, which is generated by both the stator and rotor. The fundamental equation for determining the air gap flux density from the air gap is as follows:

$$B(\theta, t) = f_{mm} \cdot \Lambda(\theta, t) \tag{9}$$

$$f_{mm} = \sum F'_n \cos(n\omega t - \theta - \beta) \tag{10}$$

For simplicity and to focus on the primary effects, only the fundamental component is considered in our analysis.

In scenarios involving rotor eccentricity, the air gap length, represented by the function $g(\theta)$, at a given position, represented by the variable θ, can be mathematically represented by the following equation:

$$g(\theta) = g_0(\theta) + \sum \delta'_{sn} \cos n(\theta + \alpha_n) - \sum \Delta'_{sn} \cos m(\theta + \alpha_m - \omega_r t) - x\cos(\theta) - y\sin(\theta) \tag{11}$$

Here, the equation for the air gap length $g(\theta)$ at position θ in the case of rotor eccentricity is refined. The first term represents the nominal air gap length at rated conditions. The second term is due to stator deformation, while the third term is a consequence of rotor deformation. The last term encapsulates the deviation of the rotor center position from its ideal position.

The relationship between Λ in Equation (9) and g in Equation (11) is as follows:

$$\Lambda(\theta) = \frac{1}{g(\theta)} \tag{12}$$

In accordance with the aforementioned conversion equation, $B(\theta, t)$ can be expressed in terms of the air gap length as follows:

$$B(\theta, t) = F'_1 \cos(n\omega t - \theta - \beta) \cdot \left(\Lambda_0 + \Lambda_s \cos\theta + \sum \Lambda_{sn} \cos(\theta + \alpha_n) + \sum \Lambda_{rm} \cos(\theta + \alpha_m - \omega_r t) \right) \tag{13}$$

In accordance with the Maxwell theory of the stress tensor, the radial force can be represented as illustrated below:

$$\sigma_n(\theta, t) = (B_n^2 - B_t^2)/2\mu_0 \tag{14}$$

Integrating $\sigma_n(\theta, t)$, the UMP can be obtained:

$$F = \oint_S \frac{1}{2\mu_0}\left(B_n^2 - B_t^2\right)dS \cdot \vec{n} + \oint_S \frac{1}{\mu_0}(B_n \cdot B_t)dS \cdot \vec{t} \tag{15}$$

Given the limited scope of the role of B_t, it can be considered an inconsequential element and thus ignored. Accordingly, the aforementioned equation can be simplified and decomposed into the following components:

$$F_x = LR \int_0^{2\pi} \sigma(\theta, t)\cos(\theta)d\theta = \frac{LR}{2\mu_0}\int_0^{2\pi} B_n^2 \cos(\theta)d\theta \tag{16}$$

$$F_y = LR \int_0^{2\pi} \sigma(\theta, t)\sin(\theta)d\theta = \frac{LR}{2\mu_0}\int_0^{2\pi} B_n^2 \sin(\theta)d\theta \tag{17}$$

Taking the static rotor eccentricity as an example, the air gap length $\Lambda(\theta)$ can be given by the following equation:

$$\Lambda(\theta) = \Lambda_0 + \Lambda_s cos\theta \tag{18}$$

Therefore, for static rotor eccentricity, considering only the first harmonic F_1' of f_{mm}, the expressions for F_x and F_y with the DC and rotating components are shown below:

$$F_x = \frac{F_1^2 RL\pi}{4\mu_0}[2\Lambda_0\Lambda_s + \Lambda_0\Lambda_s \cos(2\omega t - 2\beta)] \tag{19}$$

$$F_y = \frac{F_1^2 RL\pi}{4\mu_0}[\Lambda_0\Lambda_s \sin(2\omega t - 2\beta)] \tag{20}$$

3. Three-Dimensional Finite Element Model of Large Hydrogenerator Rotor

3.1. The Basic Structure and Parameters of Hydrogenerator

This paper's central theme concerns a substantial hydroelectric generator. This generator features a stator with an exterior diameter exceeding 18 m, a height of approximately 5 m, and a power output rating of 1000 megawatts. Its complex structure, shown in Figure 1, consists of a rotor, stator, stator frame, rotor support, upper and lower frames, magnetic poles, a magnetic yoke, and wire rods. The network model of this generator is shown in Figure 2. The stator frame stabilizes the stator core, while the rotor frame supports the rotor poles. The top and bottom frames, together with internal bearings, act as rigid supports. Table 1 outlines the basic dimensions and electrical specifications.

The circuit depicted in Figure 3 serves as a streamlined representation of a more complex system. It features three distinct phases, denoted by L_{phaseA}, L_{phaseB}, and L_{phaseC}. The line voltages, which are captured by V_a, V_b and V_c, respectively, exhibit a relationship where each is 1.732 times the corresponding phase voltage. This characteristic stems from the Wye (or Star) connection configuration. The line currents, signified by I_a, I_b, and I_c, are equivalent to the phase currents under this connection scheme. To mimic real-world conditions, the circuit incorporates resistors (R_1, R_2, R_3) and inductances (L_1, L_2, L_3). The determination of the rated load condition for the load resistance (R) and inductance (L) is a crucial aspect of the circuit's design and operation.
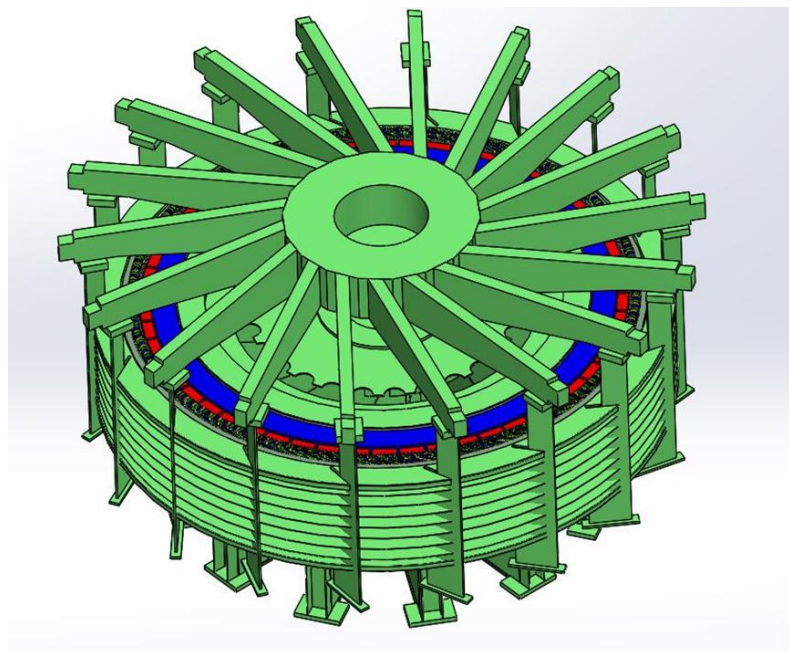
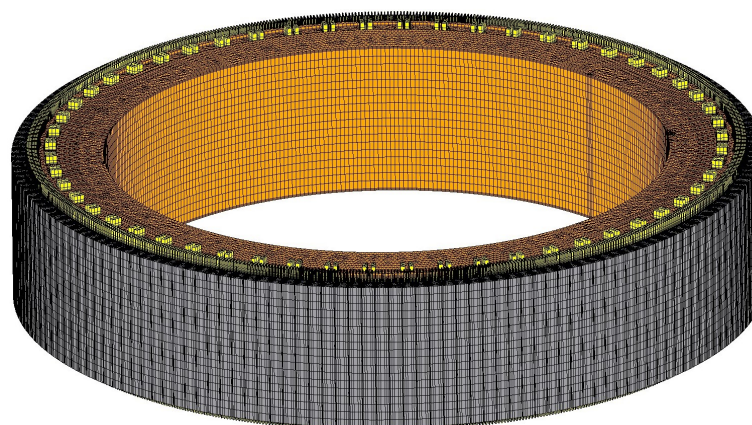**Figure 1.** Overall model of the hydrogenerator.

Figure 2. The mesh of the hydrogenerator.

Table 1. Basic parameters of the hydropower generator.

Parameters (Units)	Values
Rated power (MW)	1000
Rated power factor	0.9
Number of poles	56
Number of slots	696
Winding connection	Wye
Parallel branches	8
Coil pitch	1-12-26
Frequency (Hz)	50
Inner diameter of the stator (mm)	16,580
Outer diameter of the stator (mm)	17,190
Air gap thickness (mm)	49
The armature winding end part extension (mm)	120

$$I_N = P/(\sqrt{3}\, U_N\, cos\phi) \tag{21}$$

$$Z = \frac{U_N}{\sqrt{3}I_N} \tag{22}$$

$$R = Z cos\phi \tag{23}$$

$$Z_L = \sqrt{Z^2 - R^2} \tag{24}$$

$$L = \frac{Z_L}{\omega} \tag{25}$$

where U_N, P, I, Z, R, and L represent the rated voltage, the load of the generator, rated current, impedance, resistance, and inductance, respectively. Utilizing the aforementioned formula, it is feasible to manipulate the load impedance and inductance, thereby replicating diverse loading scenarios. Consequently, as the load conditions vary, so do the corresponding current levels and electromagnetic field distributions within the system. This approach enables the simulation and analysis of a wide range of operational states.
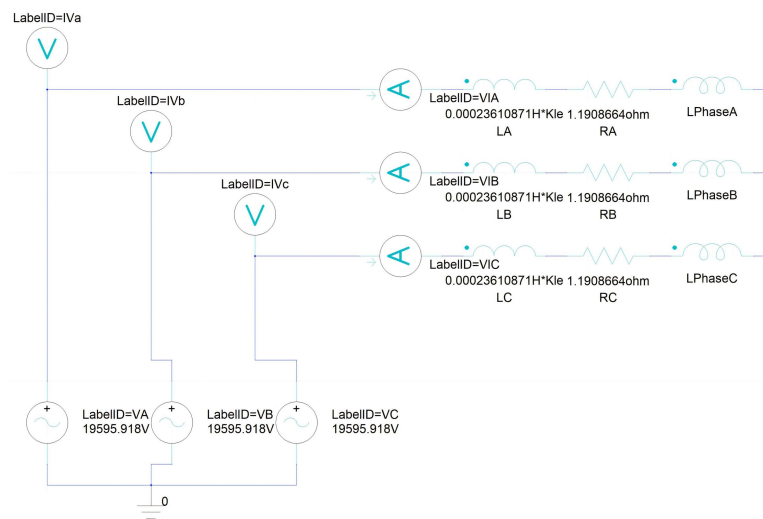
Figure 3. The external circuit of stator windings.

3.2. Model Verification

The electromagnetic field of hydrogenerator is calculated under rated working conditions. The excitation current is 3492 A, the power grid is infinite, and the output voltage of the power grid is 24 kV. The theoretical calculation formula of generator current is in the following equation:

$$I_{peak} = \sqrt{2}P/(\sqrt{3}cos\phi) \tag{26}$$

The current peak value obtained by theoretical calculation is 37.8 kA, and the current peak value obtained by finite element calculation in Figure 4 is about 37.5 kA, which verifies the accuracy of the model.

The calculated magnetic induction intensity of the air gap is shown in Figure 5 below. The distribution of magnetic induction intensity is uniform and symmetrical. According to the relevant reference data, the maximum magnetic flux density of the rotor pole is 2.05 T, the stator core magnetic flux density is 1.3062 T under load conditions, and the stator tooth groove maximum magnetic flux density is 1.8497 T under rated capacity. The magnetic density obtained by finite element calculation is 1.708 T for the magnetic pole, 1.3215 T for the stator core, and 1.8069 T for the stator tooth slot. The calculated results are basically consistent with the guaranteed values.
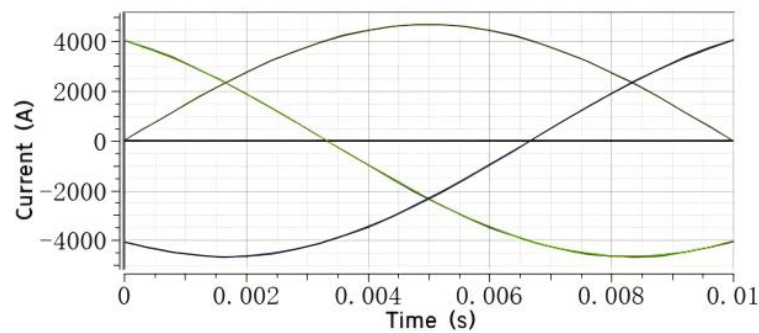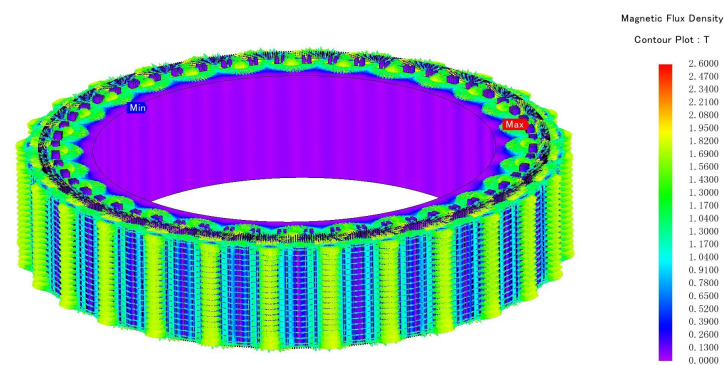
Figure 4. The current of the stator coil.

Figure 5. Magnetic induction intensity distribution of the fixed rotor of the generator.

4. Finite Element Analysis of Magnetic Pull and Magnetic Moment of Rotor Radial Eccentricity

4.1. Construction of Rotor Radial Eccentricity Model

In a standard hydrogenerator, the stator, rotor, and shaft are centered at a single point. Radial deviation means that the three centers differ in the radial direction. This section mainly considers the radial deviation of the rotor center, as shown in Figure 6. In order to ensure compliance with the installation criteria of the hydroelectric generator, it is essential to limit the allowable deviation between the rotor's center and the shaft to a maximum of 0.15 mm. In order to accommodate varying degrees of this deviation, this study has devised five distinct radial deviation models, each tailored to the specific magnitude of the deviation. The deviations are 0.05 mm, 0.1 mm, 0.15 mm, 0.2 mm, and 0.25 mm, respectively. Except the rotor deviation value, other parameters are set to be the same as those in Section 3.
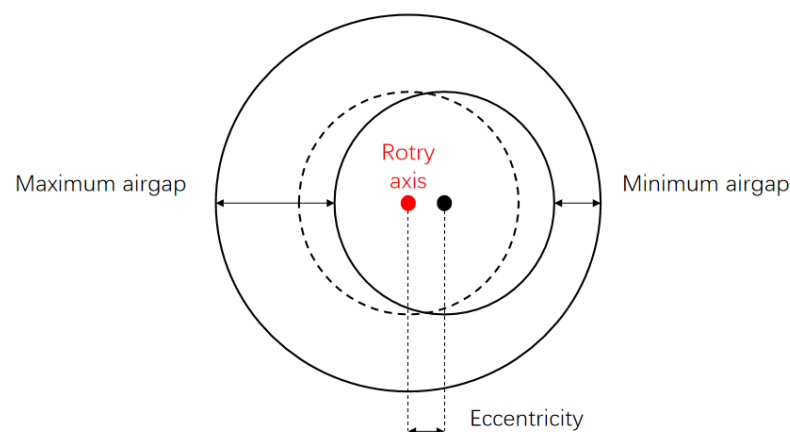
Figure 6. The schematic diagram of rotor radial eccentricity.

4.2. The Calculation and Analysis of UMP

In this section, we undertake the computation of a representative instance of rotor eccentricity configuration. Subsequently, through analyzing the derived outcomes, we delve into elucidating the underlying mechanism that governs how rotor eccentricity exerts its influence on the unbalanced magnetic attraction force within electrical generators, thereby contributing to a fresh perspective of this phenomenon.

The phenomenon of rotor eccentricity, specifically a displacement of 0.15 mm, introduces irregularities in the air gap geometry, thereby eliciting a non-uniform distribution of the magnetic field within the motor. To investigate this effect, we consider a case study of a motor operating under its nominal operating conditions, wherein the rotor exhibits an eccentricity of 0.15 mm. The subsequent analysis, utilizing the graphical representation of flux density presented in Figure 7, offers a quantitative assessment of the magnetic field's deviation from homogeneity. This academic exploration underscores the significance of understanding and mitigating rotor eccentricity to ensure optimal magnetic field distribution and, consequently, enhanced motor performance.
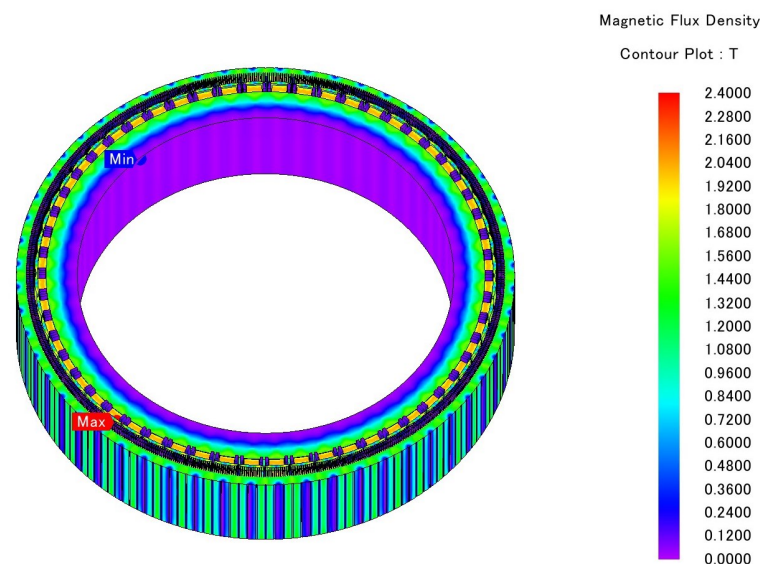
Figure 7. Magnetic induction intensity distribution under rotor eccentricity.

In the context of rotor eccentricity, the motor's magnetic field distribution exhibits a noticeable deviation from uniformity as evidenced by the flux density distribution diagram. Nevertheless, the degree of this non-uniformity remains relatively insignificant, primarily due to the minimal nature of the eccentricity. The magnetic field pattern reveals a periodic characteristic, which is inherently linked to the alternating arrangement of magnetic poles. Notably, the regions of high flux density are primarily concentrated in the vicinity of the rotor's magnetic poles, underscoring the focal point of magnetic field intensity within the motor. This academic observation highlights the intricate interplay between rotor eccentricity, magnetic field periodicity, and flux density distribution.

The generation of electromagnetic force is intimately tied to the magnetic field, with its magnitude being a direct consequence of the magnetic induction strength B. Once B is established, the density of the magnetic force can be calculated by quantifying the magnetic force applied per unit area. Subsequently, the cumulative effect of this force is obtained through integration of the force density, providing a comprehensive assessment of the electromagnetic force. This methodology is then applied specifically to the analysis of the electromagnetic force exerted on the rotor component, enabling a detailed calculation and evaluation. Figure 8, presented here, offers a graphical representation of the nodal force associated with the UMP acting upon the rotor, thereby facilitating a deeper understanding of the complex dynamics at play within the motor system.
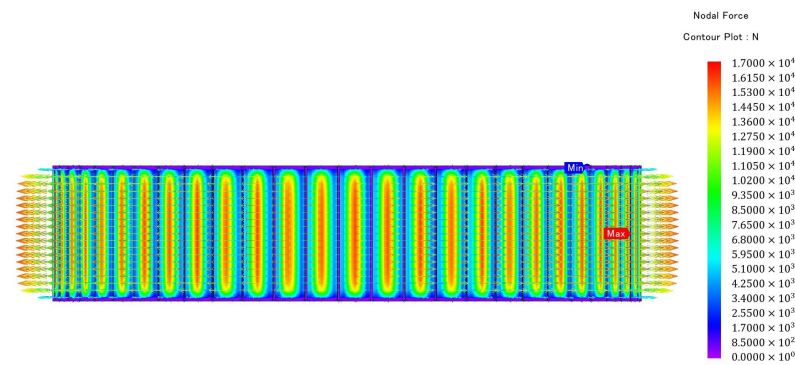
Figure 8. Unbalanced magnetic force distribution of rotor under eccentric state.

Figure 9 provides a comparison of the temporal variation in the magnitude of UMP acting on the rotor, for various levels of rotor eccentricity ranging from 0.05 mm to 0.25 mm. A discernible trend emerges from Figure 9, indicating that as the eccentricity escalates, so does the UMP on the rotor, accompanied by an intensification in the force fluctuations. To gain further insight, the unbalanced magnetic pull is subjected to Fast Fourier Transform (FFT) processing, which generates the aforementioned Figure 10. It becomes evident that the vibrational profile is intimately linked to the number of tooth slots, suggesting a complex interplay between the mechanical geometry and electromagnetic dynamics. Except for the DC component, it exists mainly at 700 Hz. The direction of the UMP follows a circumferential rotation in synchrony with the rotor velocity.

As illustrated in Figure 11, the direct current (DC) component and the primary harmonic component of the UMP are isolated and presented graphically in relation to the eccentricity values of the rotor.
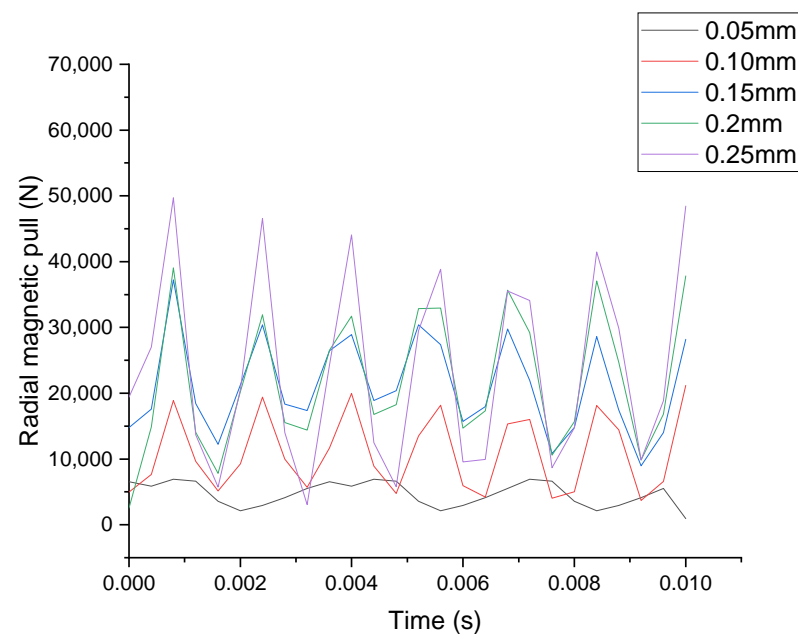
Figure 9. Plot of radial magnetic pull with time at different eccentricities.
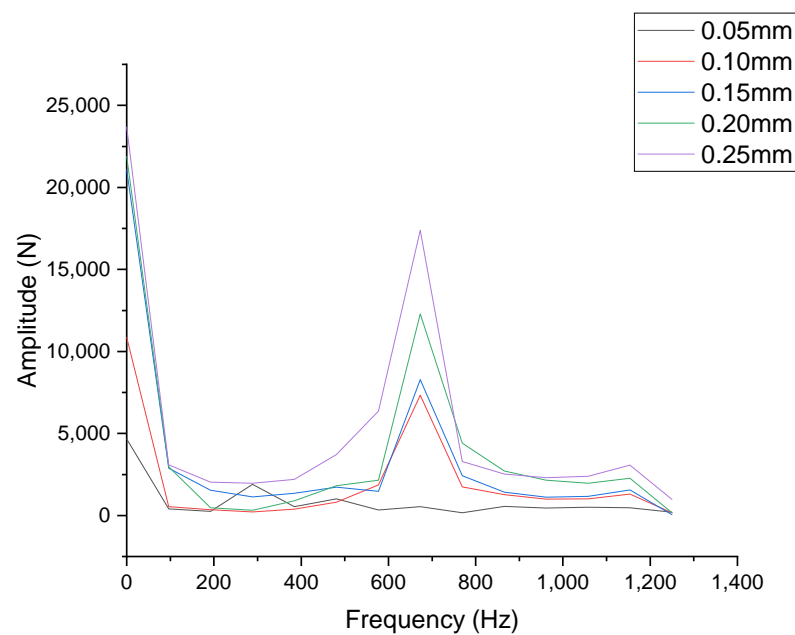
Figure 10. FFT transform of radial magnetic pull at different eccentricities.
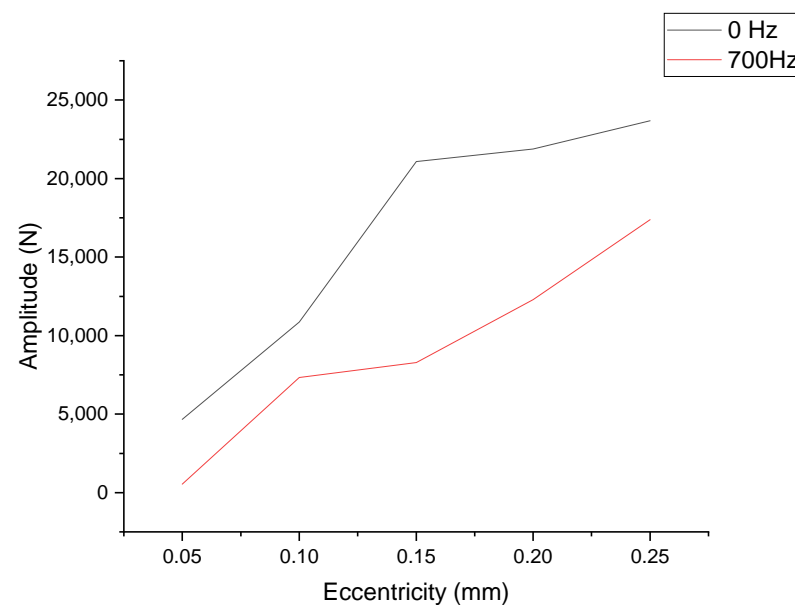
Figure 11. Plot of magnetic pull with eccentricity for different frequency components.

Upon examination of the figures, the following conclusions can be drawn in an academic context:

(1) The magnitude of the harmonic component of the UMP is markedly inferior to that of its DC counterpart, exhibiting a discrepancy that spans an entire order of magnitude. This observation highlights the dominance of the DC component in contributing to the overall electromagnetic force.

(2) A discernible trend emerges, indicating a near-linear escalation in both the DC component and the primary harmonic component of the UMP as the eccentricity increases. This variation relationship underscores the direct correlation between eccentricity and the strengthening of both the fundamental and harmonic components of the UMP acting on the rotor.

(3)   The hydrogenerator set's rotor, installed with precision, exhibits a measured eccentricity below 0.15 mm, resulting in a calculated unbalanced magnetic pull of approximately 55 t at this eccentricity level.

5. Finite Element Analysis of Magnetic Force and Torque of Rotor Axial Offset

5.1. Construction of Rotor Axial Offset Model

In a standard hydrogenerator, the stator and rotor are centered at a single point. An axial shift is when two centers are shifted in the axial direction. This section mainly considers the case where the center of the rotor shifts downward relative to the center of the stator as shown in Figure 12. According to the installation standard of the hydrogenerator, the offset between the center of the rotor and the shaft should not be more than 3 mm. In this paper, three kinds of axial offset models are designed according to the size of the offset. The offsets are 1 mm, 2 mm, and 3 mm, respectively. Except the rotor axial offset, other parameters are set as in Section 3.
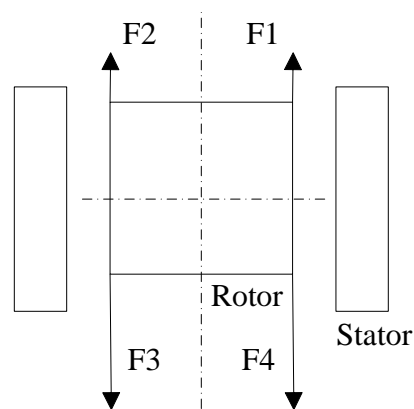
Figure 12. The schematic diagram of the rotor rotor axial offset.

5.2. The Calculation and Analysis of UMP

In this section, we undertake a comprehensive computational analysis of a representative case study focusing on the rotor axial offset. Following this, we conduct an in-depth exploration of the fundamental mechanisms that govern the influence of the rotor axial offset on the UMP inherent in electrical generators.

Firstly, the magnetic induction intensity of the generator is analyzed. The axial displacement will lead to the uniform air gap on the end face, which will lead to the uneven distribution of the magnetic field. Consider the operation of a motor with axial rotor offset of 3 mm under rated operating conditions. The following Figure 13 show the magnetic induction intensity distribution of the motor in this case. In the case of axial deflection, the axial magnetic induction intensity of the motor is not evenly distributed.

Then, we analyze the electromagnetic force of the generator. Once the magnetic induction intensity has been obtained, the electromagnetic force density per unit area can be calculated using the appropriate formula. Subsequently, the integration of this density yields the total electromagnetic force. Figure 14 below shows the nodal forces. Figure 15 shows the variation of the axial UMP of the rotor with time when the rotor axial offset is 1 mm, 2 mm, and 3 mm. As the offset increases, both the axial magnetic force and its fluctuation on the rotor increase as illustrated in the figure. Furthermore, an examination of the temporal curve of axial magnetic tension on the rotor indicates a correlation between the vibration pattern and the number of tooth slots.
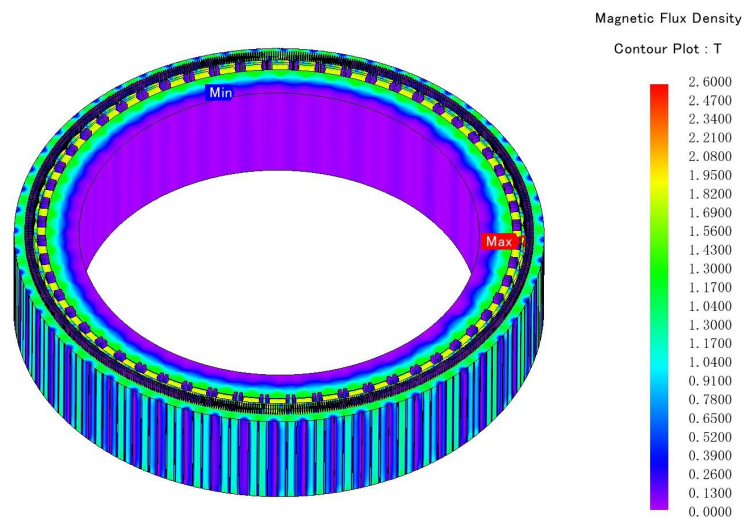
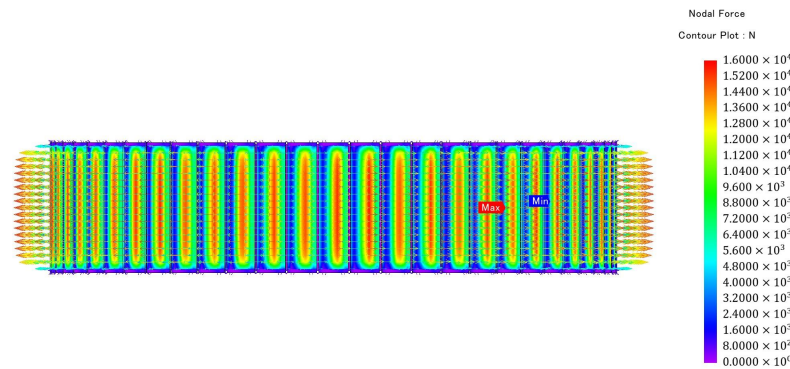**Figure 13.** Magnetic induction intensity distribution under rotor axial offset.

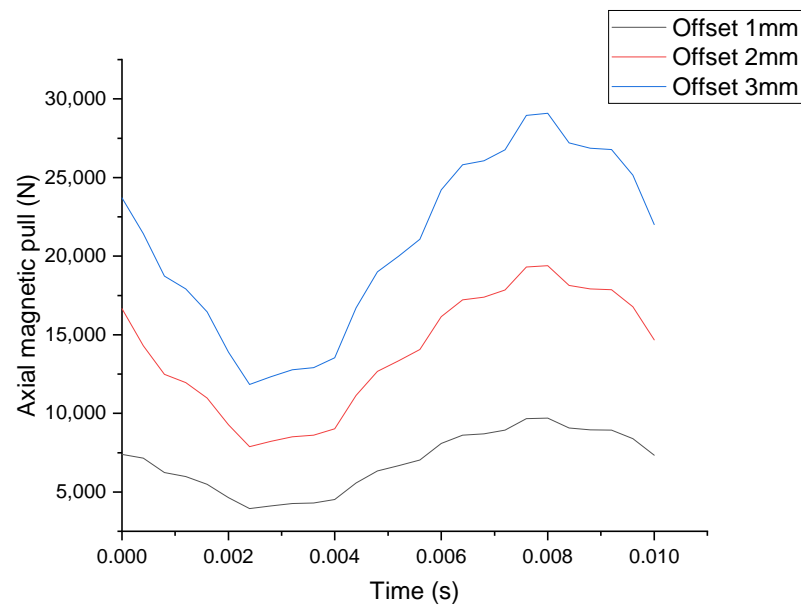**Figure 14.** Unbalanced magnetic force distribution of rotor under axial offset.

Figure 15. Plot of axial magnetic pull with time at different offset.

For further analysis, the FFT conversion of the axial magnetic tension is performed for GET as shown in Figure 16. The frequency of the axial magnetic tension is mainly caused by the harmonic component of the stator winding voltage. In addition to the DC component, the figure predominantly demonstrates the presence of the frequencies 600 Hz and 700 Hz.

It can be roughly seen from Figure 17 that with the increase in the offset, the amplitude of the DC and the main harmonics of the axial magnetic pull also increase linearly.
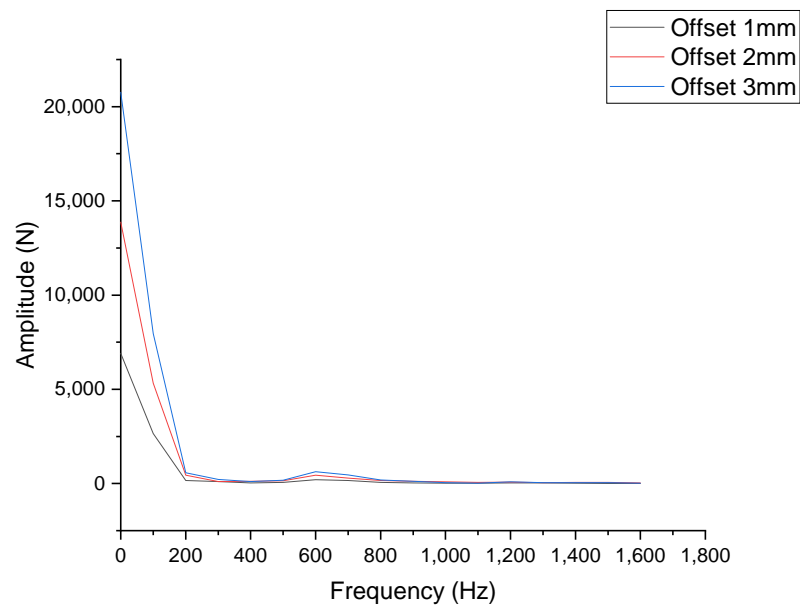
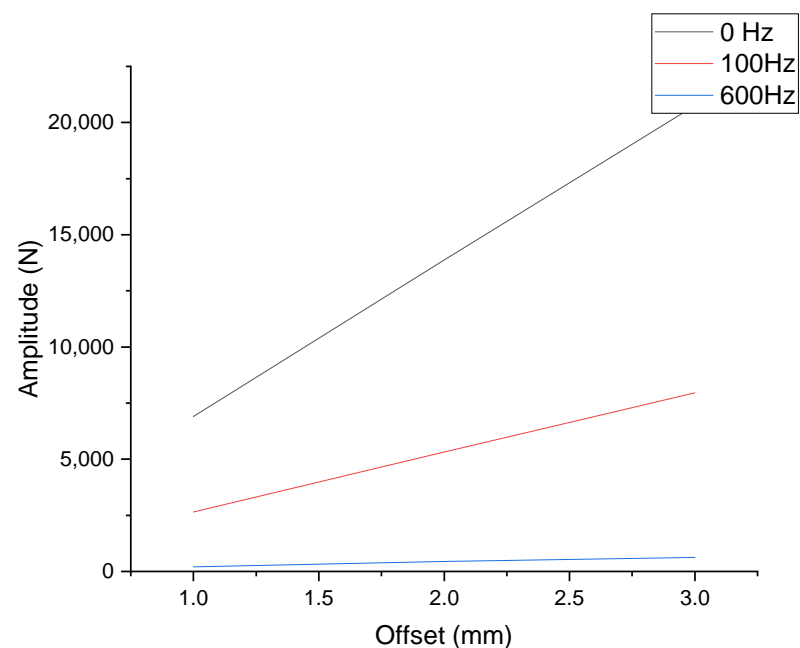**Figure 16.** FFT transform of axial magnetic pull at different offset.

**Figure 17.** Plot of magnetic pull with axial migration for different frequency components.

In summary, this section presents and discusses an accurate FEM of a 1000 MW hydroelectric generator. The model takes into account the non-uniform axial clearance between the rotor and the stator. The findings are as follows:

(1)   The axial magnetic pull will be generated after axial deviation of the rotor. The UMP direction is opposite to the offset direction. And the time distribution of the magnetic pull is related to the harmonic component of the stator winding voltage.

(2)   With the increase in the offset, the magnetic induction intensity of the upper and lower surfaces of the rotor becomes more asymmetrical, which leads to the change in the axial magnetic tension. In general, the DC component and the key harmonic component of the UMP demonstrate a nearly linear increase with the offset distance.

6. Finite Element Analysis of Axial Deflection Magnetic Force and Magnetic Moment of Rotor

6.1. Construction of Rotor Axial Deflection Model

In a standard hydrogenerator, the stator center axis, the rotor center axis, and the rotation axis coincide. Axial deflection means that the center axis of the rotor or rotation axis is deflected from the center axis of the stator. This section mainly considers the case that the central axis of the rotor is overlapped with the rotating axis but is deflected relative to the central axis of the stator as shown in Figure 18. The angle between the two is the deflection angle. According to the installation standards of the hydrogenerator, the deflection angle should not exceed 0.3°. According to the size of the deflection angle, three kinds of axial deflection models are designed. The deflection angles are 0.1°, 0.2° and 0.3°, respectively. In addition to the rotor axial deflection angle, the other parameters are set in Section 3.
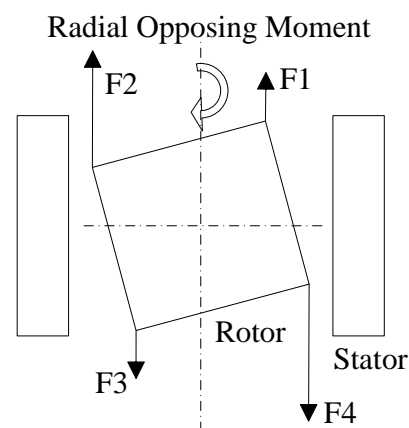
Figure 18. The schematic diagram of rotor rotor axial deflection.

6.2. The Calculation and Analysis of UMP

In this section, we undertake a comprehensive computational analysis of a representative case study focusing on rotor axial deflection. Following this, we conduct an in-depth exploration of the fundamental mechanisms that govern the influence of the rotor axial deflection on the UMP inherent in electrical generators.

Firstly, the magnetic induction intensity of the generator is analyzed. Axial deflection will result in uneven axial and radial air gaps between the stator and rotor, which will cause the non-uniform distribution of the magnetic field. Consider the operation of a motor with a rotor shaft deflection of 3° under rated operating conditions. The following Figure 19 shows the magnetic induction intensity distribution of the motor in this case. In the case of axial deflection, the axial and radial magnetic induction intensity is uneven.

Then, we analyze the UMP of the generator. Once the magnetic induction intensity has been measured, the electromagnetic force density is calculated using the appropriate formula (Figure 20) and then integrated to give the total electromagnetic force. The following Figure 21 shows the radial magnetic tension distribution of the upper, middle, and lower surfaces of the rotor of the motor along the circumference in this case. It can be seen from the figure that under the condition of shaft deflection, the radial magnetic force of the motor is unevenly distributed along the axis direction. This is caused by the uneven radial air gap when the shaft is deflected.

In addition, the deflection of the rotor shaft will produce axial magnetic tension. The distribution of magnetic tension on the upper and lower surfaces of the rotor is also different. Figure 22 below shows the distribution of the axial UMP of the generator along the circumference in this case, respectively on the upper and lower surfaces. It can be seen from Figure 22 that under the condition of shaft deflection, the axial magnetic force of the motor is unevenly distributed along the axis direction. This is caused by the uneven axial air gap when the shaft is deflected.

Further, the radial magnetic pull and axial magnetic pull are analyzed. Since the deflection point is at the center of the rotation, the resultant force of the radial magnetic pull and the axial magnetic pull is zero. However, due to the asymmetry of its distribution, the rotational torque in the radial direction will be generated. It can be seen as the torque that causes the deflection to return to the center, against the deflection. This is called the radial opposing magnetic torque, as shown in the figure. The figure shows the variation in the radial opposing magnetic torque with time when the rotor shaft is deflected by 0.1°, 0.2°, and 0.3°. It can be seen from Figure 23 that with the increase in the deflection angle, the radial opposing magnetic torque on the rotor increases. The amplitude of force fluctuations is also increasing.

For further analysis, this torque is converted by FFT, and the figure is obtained. The frequency component of the axial magnetic force due to rotor shaft deflection is mainly due to the harmonic component of the stator winding voltage. As shown in Figure 24, in addition to the DC component, a significant presence is observed at 700 Hz. It can also be seen from Figure 25 that with the increase in the deflection angle, the DC of the unbalanced magnetic force and the amplitude of the main harmonics also increase linearly.
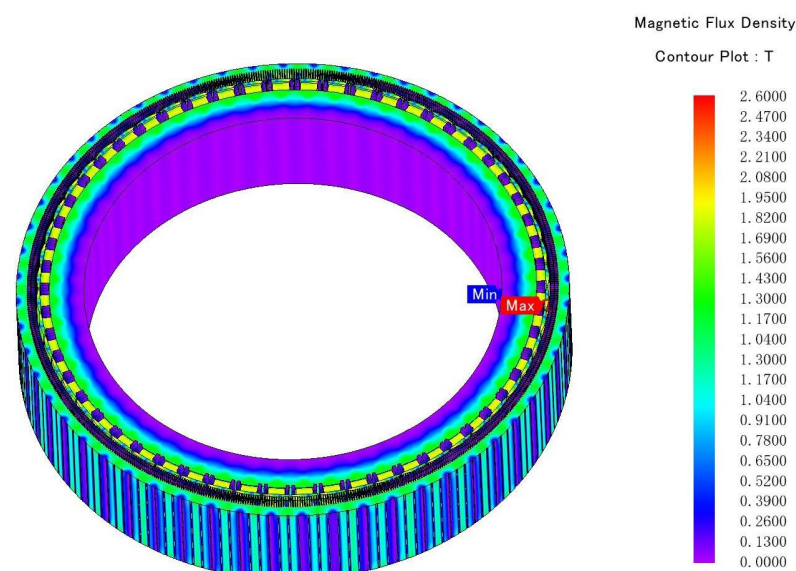

Figure 19. Magnetic induction intensity distribution under rotor axial deflection.
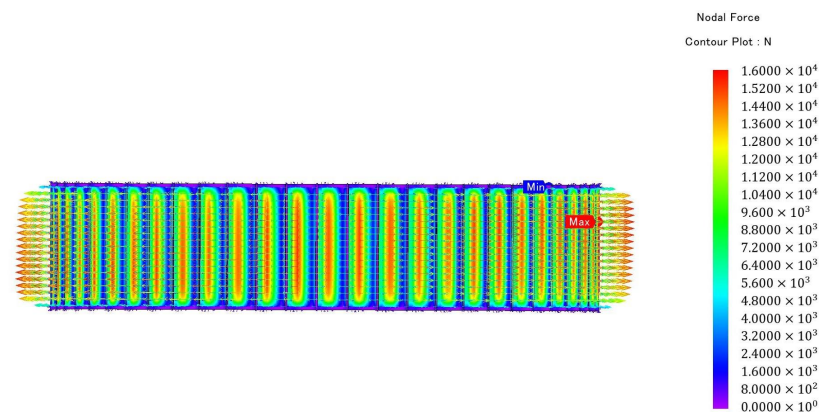

Figure 20. Unbalanced magnetic force distribution of rotor under axial deflection.

In summary, this section presents and discusses an accurate FEM of a 1000 MW hydraulic generator that takes into account the non-uniform radial and axial clearance between the rotor and the stator. The findings are as follows:

(1) After the rotor axis is deflected, the radial and axial components of UMP on different surfaces of the rotor along the axis are different.

(2) Not only does the uniformity of this magnetic pull distribution produce a radial torque against deflection but both the DC and key harmonic components of this torque increase linearly with the increase in eccentricity.
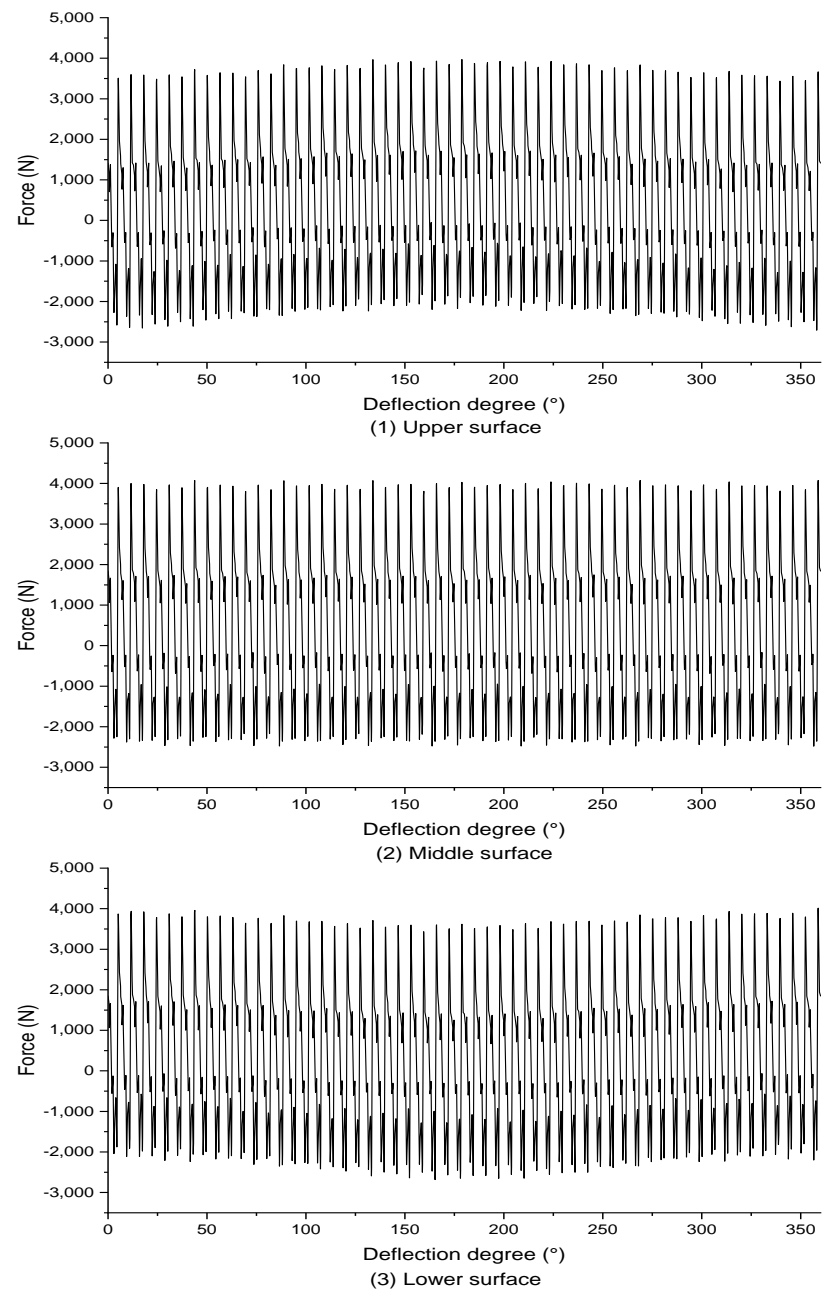
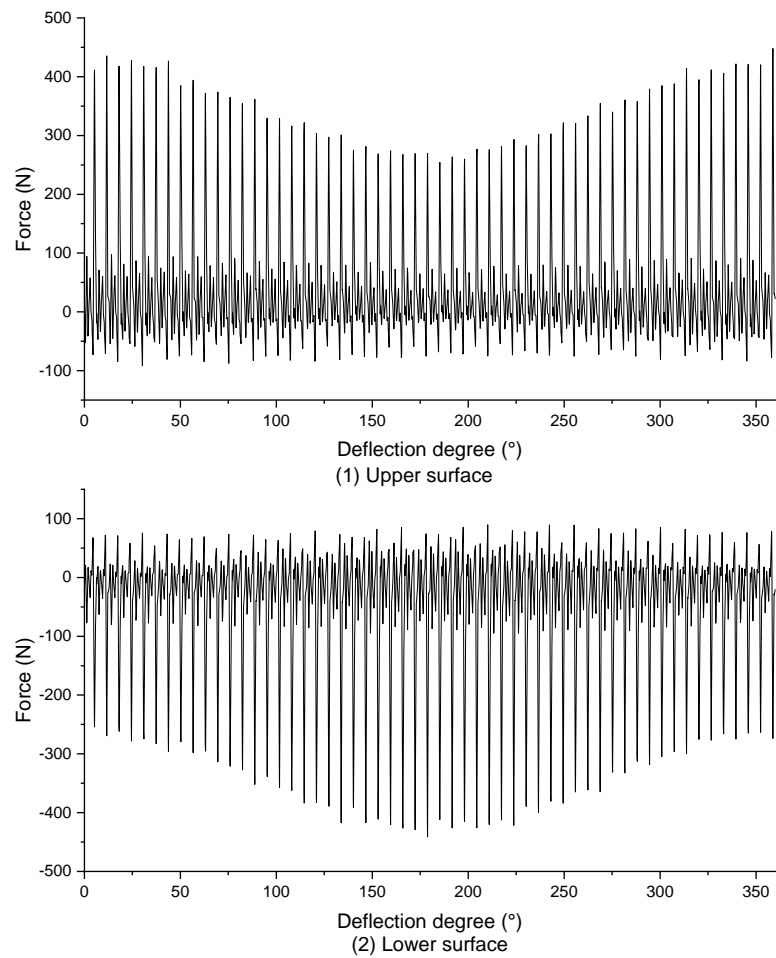**Figure 21.** Radial magnetic pull distribution of the upper, middle, and lower surfaces of the rotor.

Figure 22. Axial magnetic pull distribution of the upper and lower surfaces of the rotor.
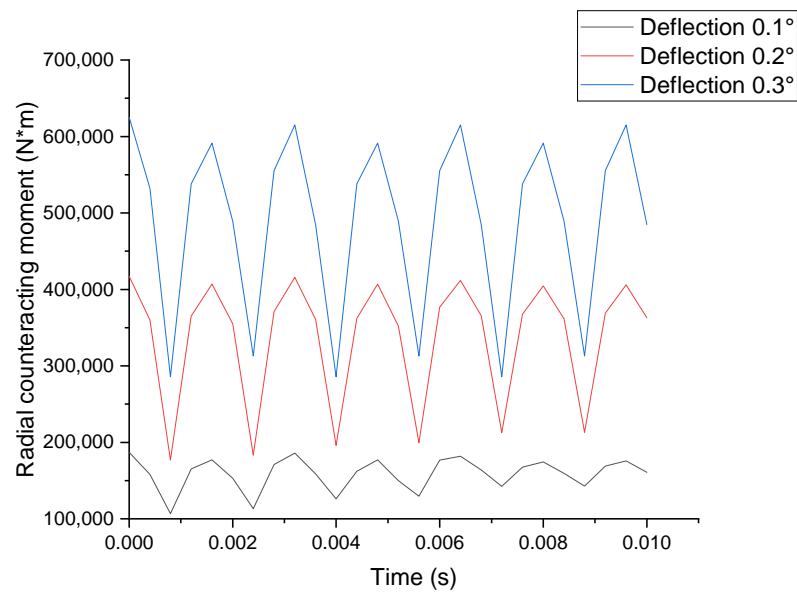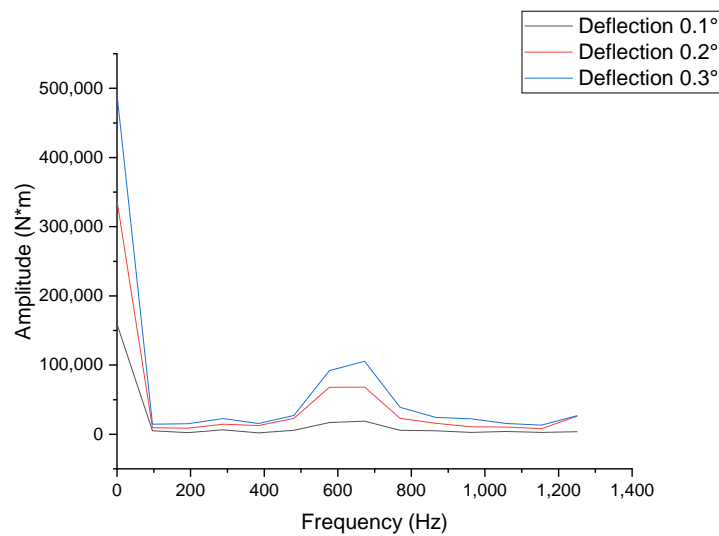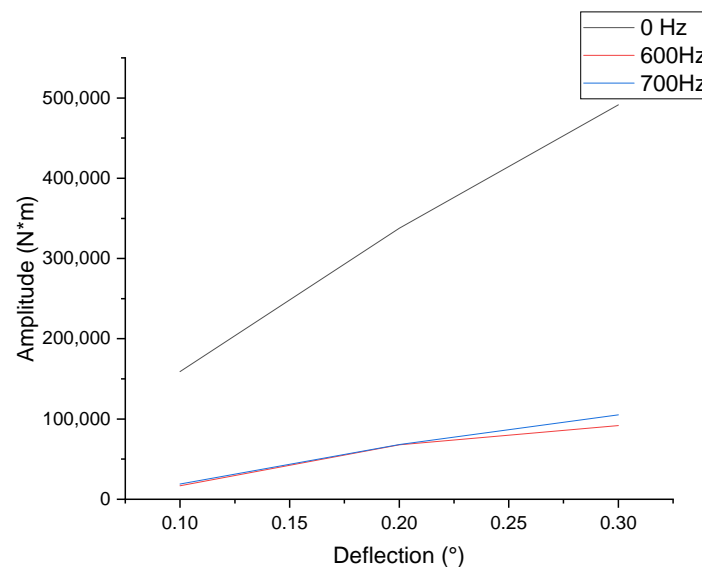
Figure 23. Plot of radial opposing magnetic torque with time at different deflection.

Figure 24. FFT transform of radial opposing magnetic torque at different deflection.

Figure 25. Plot of radial opposing magnetic torque with axial deflection for different frequency components.

7. Conclusions

In this paper, the variation law of magnetic force and torque of 1000 MW of a hydro-generator under the condition of radial eccentricity, axial deviation, and axial deflection are analyzed. The research conclusions are listed below:

- In the case of axial offset, the generator generates an axial UMP. The wave frequency of this force is related to the harmonic frequencies of the stator winding. The UMP increases linearly with the increase in the offset distance.
- In the case of axial offset, the generator generates an axial UMP. The wave frequency of this force is related to the harmonic frequencies of the stator winding. The UMP increases linearly with the increase in the offset distance.
- In the case of axial deflection, the distribution of axial and radial magnetic pulls in the generator is non-uniform at different axial positions. This results in a radial torque of rotation. The fluctuation frequency of this torque is related to the harmonic frequencies of the stator winding. The radial torque increases linearly with the increase in the deflection angle.

Future studies will take a 3D approach, including coupled calculations of the electromagnetic, thermal, and structural fields, to conduct a more detailed investigation into the effects of deviations on vibrational and deformational phenomena.

Abbreviations

The following abbreviations are used in this manuscript:

Abbreviations

DC	direct current
EMF	electromagnetic field
FE	finite element
FEM	finite element method
MST	Maxwell stress tensor
UMP	unbalanced magnetic pull
2-D	two-dimensional
3-D	three-dimensional

Nomenclature

Parameters	Description
$\mathbf{A}$	vector magnetic potential ($\mathrm{V \cdot s \cdot m^{-1}}$)
A_z	z-axis component of vector magnetic potential ($\mathrm{V \cdot s \cdot m^{-1}}$)
$\mathbf{B}$	intensity of magnetic induction (T)
B_n	tangential component of flux density (T)
B_t	radial component of flux density (T)
F	unbalanced magnetic force (N)
F'_n	the nth harmonic component of the magneto-motive force (N)
F_x	x-axis unbalanced magnetic force (N)
F_y	y-axis unbalanced magnetic force (N)
f_e	frequency of UMP with rotor eccentricity (Hz)
f_{mm}	total magneto-motive force (N)
f_r	frequency of rotor rotation (Hz)
g	air gap length (m)
g_0	average value of air gap length (m)
J	moment of inertia ($\mathrm{kg \cdot m^2}$)
$\mathbf{J}_0$	surface current density of the excitation source ($\mathrm{A \cdot m^{-2}}$)
J_{0z}	z-axis component of the surface current density ($\mathrm{A \cdot m^{-2}}$)
L	rotor length (m)
$N_{ParallelCircuit}$	numbers of the parallel circuit
N_{slots}	numbers of the tooth slots of the stator
R	rotor radius (m)
T_{em}	electromagnetic torque ($\mathrm{N \cdot m}$)

T_{load}	load torque (N$\cdot$m)
$\mathbf{v}$	movement speed (m$\cdot$s^{-1})
v_x	x-axis component of movement speed (m$\cdot$s^{-1})
v_y	y-axis component of movement speed (m$\cdot$s^{-1})
α_m	rotor phase angle (rad)
α_n	stator phase angle (rad)
β	phase angle between stator and rotor magneto-motive force (N)
$\delta_{sn'}$	air gap permeance components caused by stator deformation
$\delta_{rm'}$	air gap permeance components caused by rotor deformation
θ	angular position in the air gap (rad)
Λ	total air gap permeance (m^{-1})
Λ_{rm}	permeance of the air gap with rotor deformation (m^{-1})
Λ_s	permeance of the air gap with static eccentricity (m^{-1})
Λ_{sn}	permeance of the air gap with stator deformation (m^{-1})
Λ_0	permeance of the air gap without deformations (m^{-1})
λ	damping coefficient
μ_0	air magnetic permeability (H/m)
σ	electrical conductivity (S/m)
σ_n	radial force density (N$\cdot$m^{-2})
ω	angular velocity (rad/s)
ω_r	mechanical angular frequency (rad$\cdot$s^{-1})

References

1. Kılkış, Ş.; Krajačić, G.; Duić, N.; Rosen, M.A.; Al-Nimr, M.A. Sustainable development of energy, water and environment systems in the critical decade for climate action. *Energy Convers. Manag.* **2023**, *296*, 117644. [CrossRef]
2. Rahman, A.; Farrok, O.; Haque, M.M. Environmental impact of renewable energy source based electrical power plants: Solar, wind, hydroelectric, biomass, geothermal, tidal, ocean, and osmotic. *Renew. Sustain. Energy Rev.* **2022**, *161*, 112279. [CrossRef]
3. Isanbaev, V.; Baños, R.; Gil, C.; Gil, M.M.; Martínez, F.; Alcayde, A. Towards Energy Efficiency in Microgrids for Smart Sustainable Cities. *Lect. Notes Netw. Syst.* **2023**, *732*, 254-265.
4. Dirani Merkhouf, A.; Giroux, A.-M.; Kedjar, B.; Al-Haddad, K. Impact of Real Air-Gap Nonuniformity on the Electromagnetic Forces of a Large Hydro-Generator. *IEEE Trans. Ind. Electron.* **2018**, *65*, 8464–8475. [CrossRef]
5. Song, Z.; Liu, Y.; Guo, P.; Feng, J. Torsional Vibration Analysis of Hydro-Generator Set Considered Electromagnetic and Hydraulic Vibration Resources Coupling. *Int. J. Precis. Eng. Manuf.* **2018**, *19*, 939–945. [CrossRef]
6. Zhou, J.; Peng, X.; Li, R.; Xu, Y.; Liu, H.; Chen, D. Experimental and Finite Element Analysis to Investigate the Vibration of Oblique-Stud Stator Frame in a Large Hydropower Generator Unit. *Energies* **2017**, *10*, 2175. [CrossRef]
7. Verez, G.; Barakat, G.; Amara, Y. Influence of slots and rotor poles combinations on noise and vibrations of magnetic origins in 'u'-core flux-switching permanent magnet machines. *Prog. Electromagn. Res. B* **2014**, *61*, 149–168. [CrossRef]
8. Hu, Q.L.; Xiao, K.; Zhou, Z.T.; Fan, Z.N.; Yang, Y.; Bian, Z.Y.; Li, J.C.; Yao, B. 3D Transient Electromagnetic-Temperature Field Analysis of the Loss and Heat of the Damper Bars of a Large Tubular Hydro-Generator During Short Circuit Faults. *IEEE Access* **2020**, *8*, 135963–35974. [CrossRef]
9. Wang, L.; Li, W. Assessment of the Stray Flux, Losses, and Temperature Rise in the End Region of a High-Power Turbogenerator Based on a Novel Frequency-Domain Model. *IEEE Trans. Ind. Electron.* **2018**, *65*, 4503–4513. [CrossRef]
10. Jiang, H.C.; He, Y.L.; Tang, G.J.; Yuan, X.H. Electromagnetic Force and Mechanical Response of Turbo-Generator End Winding under Electromechanical Faults. *Math. Probl. Eng.* **2021**, *2021*, 1–19. [CrossRef]
11. Wang, L.; Cheung, R.W.; Ma, Z.; Ruan, J.; Peng, Y. Finite-Element Analysis of Unbalanced Magnetic Pull in a Large Hydro-Generator Under Practical Operations. *IEEE Trans. Magn.* **2008**, *44*, 1558–1561. [CrossRef]
12. Nasiri-Zar, I.R.; Toulabi, M.S.; Karami-Shahnani, A. Two-Segment Magnet Transverse Flux Ferrite PM Generator for Direct-Drive Wind Turbine Applications: Nonlinear 3-D MEC Modeling and Experimental Validation. *IEEE Trans. Energy Convers.* **2022**, *37*, 1834–1843.
13. Nuzzo, S.; Galea, M.; Gerada, C.; Brown, N. Analysis, Modeling, and Design Considerations for the Excitation Systems of Synchronous Generators. *IEEE Trans. Ind. Electron.* **2018**, *65*, 2996–3007. [CrossRef]
14. Xu, Y.; Zhao, D.; Wang, Y.; Ai, M. Electromagnetic Characteristics of Permanent Magnet Linear Generator (PMLG) Applied to Free-Piston Engine (FPE). *IEEE Access* **2019**, *7*, 48013–48023. [CrossRef]
15. Zhu, S.; Liu, C.; Wang, K.; Zhou, Z.; Yu, J. Structure and Operating Performance of a Double Electrical Excitation Synchronous Generator With Embedded Brushless Synchronous Exciter Utilizing DC-Field Excitation. *IEEE Trans. Energy Convers.* **2022**, *37*, 50–64. [CrossRef]
16. Li, Y.B.; Ho, S.L.; Fu, W.N.; Liu, W.Y. An interpolative finite element modeling and its starting process simulation of a large solid pole synchronous machine. *IEEE Trans. Magn.* **2009**, *45*, 4605–4608. [CrossRef]
17. Mirimani, S.M.; Vahedi, A.; Marignetti, F.; Di Stefano, R. An online method for static eccentricity fault detection in axial flux machines. *IEEE Trans. Ind. Electron.* **2015**, *62*, 1931–1942. [CrossRef]

18. Karlsson, M.; Aidanpää, J.O.; Perers, R.; Leijon, M. Rotor Dynamic Analysis of an Eccentric Hydropower Generator With Damper Winding for Reactive Load. *J. Appl. Mech.* **2007**, *74*, 1178–1186. [CrossRef]

19. Li, R.; Li, C.; Peng, X.; Wei, W. Electromagnetic Vibration Simulation of a 250-MW Large Hydropower Generator with Rotor Eccentricity and Rotor Deformation. *Energies* **2017**, *10*, 2155. [CrossRef]

20. Calleecharan, Y.; Aidanpaa, J.O. On the Dynamics of an Hydropower Generator Subjected to Unbalanced Magnetic Pull. In Proceedings of the IET 8th International Conference on Computation in Electromagnetics (CEM 2011), Wroclaw, Poland, 11–14 April 2011; pp. 50–51.

21. Calleecharan, Y.; Jauregui, R.; Aidanpää, J.O. Estimating forces in mixed eccentricities motion from purely dynamic eccentric rotor centre motion in a hydropower generator and their validation against EM simulations. *Balk. J. Electr. Comput. Eng.* **2015**, *3*. [CrossRef]

22. Ma, M.; Li, Y.; Wu, Y.; Dong, C. Multifield Calculation and Analysis of Excitation Winding Interturn Short Circuit Fault in Turbo-Generator. *Energies* **2018**, *11*, 2626. [CrossRef]